SAND2014-15132J

Validating density functional theory (DFT) simulations at high energy-density conditions with liquid krypton shock experiments to 850 GPa on Sandia's Z machine

Thomas R. Mattsson,* Seth Root,† Ann E. Mattsson,‡ Luke Shulenburger,§ Rudolph J. Magyar,¶ and Dawn G. Flicker**
Sandia National Laboratories, Albuquerque, New Mexico 87185, USA
(Dated: June 18, 2014)

We use Sandia's Z machine and magnetically accelerated flyer plates to shock compress liquid krypton to 850 GPa and compare with results from Density Functional Theory (DFT) based simulations using the AM05 functional. We also employ Quantum Monte Carlo (QMC) calculations to validate the use of AM05. We conclude that the DFT results are sensitive to the quality of the pseudopotential in terms of scattering properties at high energy/temperature. A new Kr projector augmented wave (PAW) potential was constructed with improved scattering properties which resulted in excellent agreement with the experimental results to 800 GPa and temperatures above 10 eV (110 kK). Finally, we present comparisons of our data from the Z experiments and DFT calculations to current EOS models of krypton to determine the best model for high energy density applications.

PACS numbers: 62.50.Ef,71.15.Pd,82.35.Lr

I. INTRODUCTION

Density Functional Theory (DFT)[1] has emerged as the method of choice for first-principles simulations of material's properties under high energy-density conditions, for example the extreme pressures and temperatures reached under shock compression. There are now many examples of accurate DFT simulations compared to high precision experimental data, primarily from first and second row elements and compounds like hydrogen[2], carbon[3] , quartz[4], water[5], and carbon dioxide[6]. Although DFT is a formally exact reformulation of the quantum mechanical many-body problem, providing a path to observables via density functionals, different types of approximations enter during the course of performing large-scale quantum molecular dynamics (QMD) simulations. Considerable interest exists in validating calculations for elements with higher atomic number in regimes of high density, temperature, and pressure.

The properties of krypton make it ideal to study these effects on heavier elements; the initial state of cryogenically-cooled liquid krypton is well known. Upon shock compression, krypton turns metallic, resulting in a reflective shock front, allowing for very high precision measurements of the shock velocity. Few experimental data on krypton at high pressures exist, with prior Hugoniot data limited to just below 100 GPa. Obtaining data in the range of several hundreds of GPa would provide knowledge of the behavior of krypton at a significantly increased range in density, temperature, and pressure.

In addition to the broad experimental motivation for this work, our initial DFT krypton Hugoniot calculations indicated that the standard projector augmented wave (PAW) potential distributed with VASP was inadequate at the high pressures and temperatures occurring under strong shock compression, raising important questions about verificiation of PAW potentials and validation of QMD as a method in general at very high temperatures. In this article, we describe an approach to evaluating and constructing PAW potentials with high fidelity for application to high pressure, density, and temperature. We furthermore examine the liquid krypton Hugoniot to pressures of 800 GPa using QMD and present quantum Monte Carlo (QMC) calculations on liquid krypton. Finally, we present data from shock compression experiments on Sandia's Z machine. Following the introduction is a section on employing DFT for simulations under high energy-density (HED) conditions with emphasis on construction of high quality PAW potentials and using QMC calculations to compare functionals, a section describing the design, diagnostics, and analysis of shock experiments on Z, and finally a section devoted to results and discussions.

II. FIRST-PRINCIPLES SIMULATIONS: DFT AND QMC

DFT[1] is a formally exact reformulation of the quantum mechanical many-body problem that results in a significant reduction in computational complexity compared to methods that rely on direct solutions of the Schrodinger equation. The approximations necessary to perform simulations of hundreds of atoms and how to systematically converge the calculations are discussed in detail in Ref. 7. In this article, we will discuss two aspects: the choice of exchange-correlation (XC) functional and the construction of PAW core potentials with high fidelity for use at high temperature.

A. Selecting an Exchange Correlation Functional

The most important fundamental approximation in any DFT calculation is the choice of an approximate XC functional. The XC functional incorporates all many-

body quantum physics effects and via its functional derivative with respect to density, in turn, incorporates these into an effective potential for independent particles. We look to choose between two complementary functionals: LDA and AM05[8]. LDA is expected to perform accurately in the high density limit where the electron distribution is close to uniform while the AM05 functional includes a dependence on the dimensionless gradient in addition to the density and is designed to capture the effects of surfaces by matching results for a surface system, the Airy gas[9]. In the high density limit the functional approaches LDA. AM05 has a high fidelity for several classes of solids[10,11] under normal conditions and its performance under shock compression is also excellent. For example, AM05 has been validated for shock compression of compressed SiO_2 to 1700 GPa[4].

Importantly for this work, AM05 shows a complete absence of van der Waals (vdW) attraction[11]. The result is monotonic predictable behavior for low density allowing for more straightforward inclusion of vdW, if necessary, than functionals where an incorrect attraction first has to be compensated for.

No a priori way exists for choose which density functional will most accurately reproduce the many body physics of a given system, be it of atomic, molecular, or condensed matter character. In the case of krypton, strong a posteriori clues due to prior work on the xenon Hugoniot[12] suggest that the AM05 functional[8] will perform well. However, the handling of the initial (relatively low pressure and cryogenic) state of these calculations causes some concern given that AM05 by design will not bind solid noble gases. Ideally as we are after thermodynamic properties, we would like to choose a functional that can at least reproduce the proper dynamics of the ions under all temperatures and pressures we consider. In a canonical ensemble where the particle number, density and temperature are held fixed (NVT), the ionic configurations should be sampled from a Boltzmann distribution. The probability of sampling any state of the system is then dependent only on the relative energies of those states. So if the functional can reproduce the relative energy ordering of different ionic configurations this will increase confidence that the dynamics are accurate.

To test the accuracy of the various density functionals for the low temperature initial state of krypton, we apply the explicitly many-body diffusion quantum Monte Carlo method (DMC) which is a method for solving the Schrodinger directly. In this computational technique there is no effective Hamiltonian and long range interactions are evaluated exactly, rendering it an excellent choice for the study of materials where van der Waals interactions are important[13]. In performing DMC calculations of krypton, we use the same pseudopotentials and other methodology as was recently reported in Ref. 14 which found excellent agreement with hydrostatic pressure experiments for the bulk modulus and x-ray diffraction experiments for the equilibrium lattice constant once zero point motion is considered[15,16].

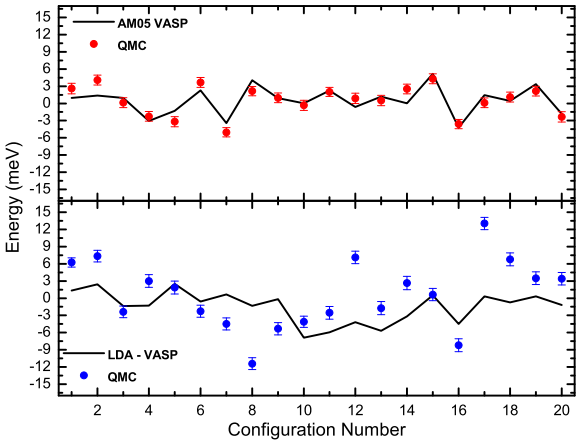

FIG. 1. (color online) Relative energies of snapshots of 32 atom cells of Kr at 118K and 2.43 g/cc. The top panel compares DMC energies of snapshots extracted from AM05 calculations to the AM05 energetics. The bottom panel shows the same for snapshots extracted from LDA based QMD simulations. The poor agreement is due to clumping of the liquid.

In choosing an appropriate functional for shocked liquid krypton, we compare two different density functionals, the local density (LDA)[17] and Armiento-Mattsson (AM05)[8]. To accomplish this comparison, we extracted snapshots of the atomic positions and total energy from 32 atom QMD simulations at the density (2.43 g/cc) and temperature (118 K) corresponding to the initial state of the krypton fluid used in the shock compression experiments. In each case, we compare the relative energetics to those obtained using DMC as performed by the qmcpack code[18]. The two functionals show a marked difference (Fig. 1), with the energetics from AM05 tracking those calculated with DMC and the LDA results having an altogether different behavior. Additionally, the spread of the energies in the case of the LDA indicates that even if the ionic configurations were representative of the proper fluid, the energetics correspond to a system at a higher temperature than the 118K desired. The reason for this behavior is that the condition of these simulations correspond to a negative pressure state in LDA and as a result, the atoms tend to form clumps rather than exhibiting liquid-like behavior. These results, coupled with the results for xenon under shock compression[12] provide convincing validation for the applicability of AM05 to the krypton Hugoniot. The combination of DFT and QMC offers a general approach to improve the predictive capability of DFT simulations; A particularly important aspect for modeling materials where properties are unknown and experiments are difficult, expensive, or perhaps even impossible to perform. A similar methodology has also been used recently to assess functionals for use with dense hydrogen and water[19,20]

B. Construction and Validation of PAW potentials

The second necessary approximation for performing large-scale molecular dynamics simulations that determines forces and energies from DFT calculations is the use of core-potentials to remove the need to include large numbers of electrons in the calculations. In practice, chemically inert core electrons are replaced by a pseudopotential (PP) and only the valence electrons are treated explicitly. High quality PPs are available for VASP[21] and other codes. The quality is usually determined by comparing zero temperature lattice constants and bulk moduli with results from equivalent calculations with an all-electron code. It is important to note that the quality of a PP can only be determined by comparison to all-electron calculations and never by comparison to experiment. The key issue is ensuring their transferability. A PP is usually constructed from the all-electron results of a single, free, spherically symmetric atom. For this atom the PP generally produces the same results as an all-electron calculation. However, the success of transferring a PP to a different environment, such as to an atom in a bulk lattice, is dependent on a number of factors. Until recently most PPs have been constructed for bulk matter at equilibrium and at fairly low temperatures. We use the projector augmented-wave (PAW) PPs distributed with VASP. While these PPs usually produce very good zero temperature equilibrium lattice constants and bulk moduli, the accuracy may not hold for high energy density applications. The use of these PAWs constructed for low temperatures in extreme environments can produce less reliable results, as evident in this work and previous work on xenon[22].

Additional considerations needed for using PPs at high temperature and pressure are illustrated in Fig. 2. In Fig. 2 we plot the arc tangent of the logarithmic derivative at R,

$$\frac{d\log\phi(r)}{dr}|_{r=R} = \frac{d\phi(r)}{dr}/\phi(r)|_{r=R}\,, \qquad (1)$$

of radial wave functions of different angular momentum versus the energy of the wave function, calculated in the krypton atom with the PAW potential (colored dotted lines) compared to the all-electron results (black/gray dotted lines). Fermions (electrons) occupy states around the Fermi energy according to the temperature dependent Fermi-Dirac distribution. As seen in Figure 2 the distribution at high temperature (black full line, $180000K$) is considerably wider than at room temperature (gray dashed line). The quality of the wave functions above the Fermi energy thus need to be much higher at larger temperatures. It is clear that the standard PAW potential in a) is not suitable for larger temperatures while being adequate for low temperatures.

We constructed[23] a new PAW potential for krypton from the same 8 valence electron atomic configuration as the standard potential, using the f atomic orbital for the local potential instead of the d, decreasing the partial core radius from 2.00 to 1.80 bohr, and adding projectors to both the p and d channels. The pertinent information for the projectors is summarized by a giving the energy and the cut-off radius from the description field in the VASP POTCAR file:

```
Description
  l       E           RCUT
  0    -23.1713547    1.800
  0    -16.3269912    1.800
  1     -9.3927349    2.000
  1      1.3605826    2.000
  2     -1.3605826    2.300
  2     27.2116520    2.300
  3     -1.3605826    2.300
```

where l is the angular momentum of the given projector, cut-off distances (RCUT) are in bohr, and projector energies (E) in eV. This results in the PAW potential with the same outmost cutoff radius of 2.30 bohr and a slightly larger recommended kinetic energy cut-off (ENMAX 239.322 vs. 185.392 eV), used in Fig. 2 b). Comparing Fig. 2 a) and b) an improvement is evident, particularly in the p and f channels. This PAW potential is adequate for considerably higher temperatures compared to the standard PAW potential used in a).

While the new Kr PAW potential might be adequate for the temperatures reached in our calculations, the very high pressure conditions need to be taken into account as well. It is important to consider if the inert core approximation is valid at these higher temperatures and pressures. A concern was that the lowest valence electron energy levels in the calculations were not fully occupied in our calculations. That is, the Fermi-Dirac distribution at these high temperatures also affected the lowest energy electrons explicitly included in the calculations. Depending on the electronic structure, this may be a sign of including too few valence electrons. In addition, when investigating the average particle distance we found that a substantial fraction of the electrons were closer than two times the outmost core radius of the potential[23]. Again, overlap does not automatically disqualify a potential, but these two occurrences suggest that the electrons in the highest lying core levels are not inert and we need to add them to the valence in order to treat them explicitly and reduce the core radii.

In Fig. 2 c) we show the results at the smaller R of 2.0 bohr, from the new PAW potential where the 10 d-electrons are added to the valence. The partial core radius is decreased further to 1.40 bohr, and all cut-off radii are reduced and projectors added:

```
Description
  l       E           RCUT
  0    -23.1713547     1.500
  0     -9.5240782     1.500
  0    129.2553470     1.600
  1     -9.3927349     1.700
  1     -4.0817478     1.700
```

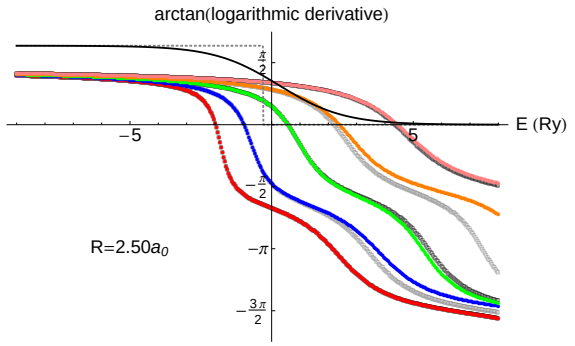

a) Standard (8 electron) Kr PAW (PAW Kr 07Sep2000)

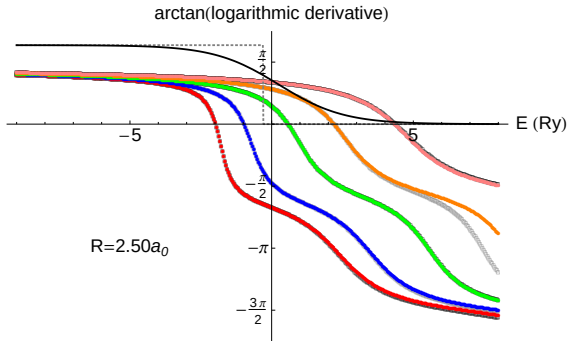

b) New 8 electron Kr PAW

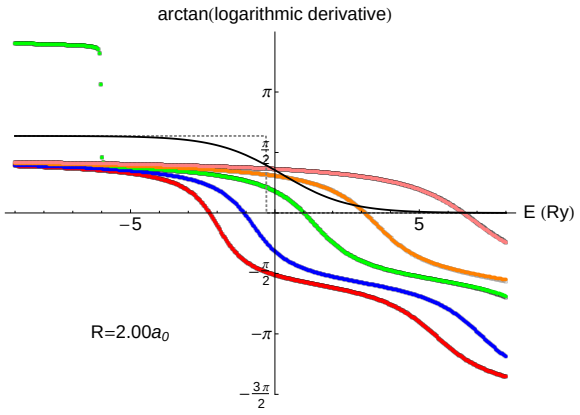

c) New 18 electron Kr PAW

FIG. 2. Logarithmic derivatives of atomic radial wave functions at distance R from the nucleus as a function of energy. Colored lines are s (red), p (blue), d (green), f (orange), and g (pink) angular momentum solutions from a pseudopotential calculation. They are compared to the corresponding black/gray all-electron solutions. The black full (gray dashed) line shows the Fermi-Dirac distribution at $180000K$ ($300K$) with the Fermi energy that of an isolated atom.

```
1     102.0436950      1.900
2     -81.7651686      1.500
2      -1.3605826      1.500
2      27.2116520      1.600
3      -1.3605826      1.600
```

The resulting plane-wave cut-off energy ENMAX is almost tripled; 680.776 eV, and the outmost core radius reduced to 1.90 bohr, a value more commensurate with the high densities in our calculations. As seen in Figure 2 c) the logarithmic derivatives are improved considerably even at this smaller distance from the nucleus, and this PAW potential should be adequate for all calculations here presented. Note that the Fermi-Dirac distribution for very large temperatures, in fact, reaches down to the distinct step feature at ~ -6 Ry (-81.76 eV) marking the very narrow band of $3d$ (core) levels. However, with this potential, more of the electrons need to be explicitly treated in the calculations and it also requires a higher kinetic energy cut-off making it more computationally expensive.

Good agreement between the logarithmic derivatives of the wave-functions in PP and all-electron calculations on an atom is a necessary but not sufficient condition of appropriateness. Further testing should be considered, such as the usual calculations of equilibrium properties of a solid. For our applications it is also valuable to compare density of states for some relevant atomic configurations calculated with the PP and compared to an all-electron calculation[23], in particular to identify ghost states at high energies.

Having investigated the fidelity of the PAW core-functions and assessed the fidelity of the exchange correlation functional we are now in a position to perform DFT simulations with confidence. The next section describes the molecular dynamics simulations.

C. Quantum Molecular Dynamics

The DFT-MD simulations were performed with VASP 5.3.3[24] using stringent convergence settings[7,22]. Electronic states were occupied according to Mermin's finite-temperature formulation of DFT[25], which is essential for performing QMD simulations with high fidelity in the warm dense matter regime[2,7]. The shock experiments generate a Hugoniot curve, the loci of end states reached in a single shock, defined with respect to a given reference state.

The reference state for the calculations is the experimental initial conditions of liquid krypton at a density of 2.43 g/cm^3 at T=118 K. The hydrostatic Hugoniot condition is expressed as $2(E-E_{ref}) = (P-P_{ref})(v_{ref}-v)$ with E the internal energy per atom, P the system pressure, and v the volume per atom. E_{ref} and P_{ref} are the energy and pressure in the initial state. The Hugoniot points were calculated by performing simulations at several temperatures for each density of interest for low and medium compression, while keeping the temperature fixed and changing the density in small increments, for the steep section of the Hugoniot where the shock pressure is not as sensitive to the temperature as it is to the density. A change from temperature to density increments significantly improves numerical convergence in the high temperature regime. A typical fully thermalized simulation requires of the order 4000 to 8000 time steps.

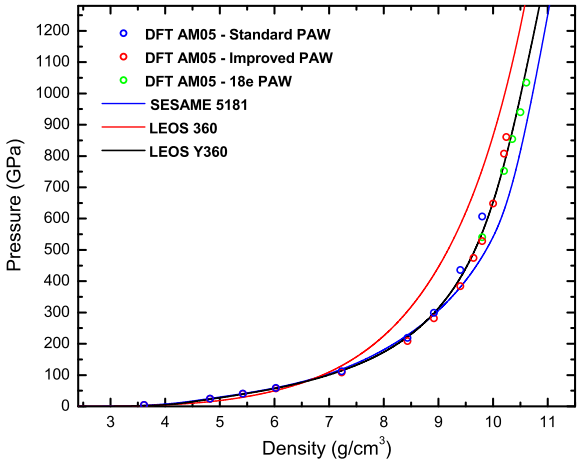

FIG. 3. Shock Hugoniot of liquid krypton calculated with different PAW potentials using the AM05 XC functional together with tabular equation of state models.

The velocity Verlet algorithm was used with a time-step ranging from 0.5 fs to 4 fs depending on temperature, maintaining stable ionic trajectories requiring of the order 3 to 10 electronic iterations per ionic step. The results from QMD simulations are shown in Section II B and IV A.

As predicted in Section II B, initial DFT Hugoniot calculations on krypton indicated that the standard PAW potential distributed with VASP was inadequate at high pressures and high temperatures occurring under shock compression. Fig. 3 shows the standard PAW gives a significant steepening of the Hugoniot at high compression, very similar to the behavior seen for the standard xenon potential[22]. Two new krypton PAW potentials were therefore constructed, both with improved scattering properties for the atom at high energies, see Fig. 2, and a behavior in pressure that agrees with experimental data. The simulation results for the principle Hugoniot are listed in Table I.

III. SHOCK EXPERIMENTS ON SANDIA'S Z MACHINE

The high P–T response of liquid Kr was determined through shock compression experiments performed on the Sandia Z-accelerator.[26] Z is a pulsed power accelerator capable of producing currents and magnetic fields greater than 20 MA and 10 MG. The large current and field densities generate magnetic pressures up to ∼650 GPa that can accelerate flyer plates up to 40 km/s.[27] The use of Z for performing shock experiments has been demonstrated for a wide range of materials and validated against traditional plate impact methods[28,29]

TABLE I. QMD calculations of the principal Hugoniot for shock compressed liquid krypton with an initial density of $2.43 g/cm^3$. The points in the table are the calculated thermodynamic state of the krypton in the post shock state. The AM05 XC functional was used in all calculations. At lower pressures the improved PAW with 8 electrons in the valence was used. At higher pressures, the PAW with 18 electrons in the valence was used.

Density (g/cc)	Pressure (GPa)	Temperature (K)
3.615	4.0	700
4.82	24.3	8000
5.42	39.9	13000
6.025	57.6	17500
7.23	108	28600
8.917	282	48750
9.399	384	80000
9.64	474	94000
9.8*	540	104000
10.2*	752	134000
10.35*	854	146000
10.50*	940	157000
10.61*	1035	170000

* Indicates calculations performed using the 18 electron PAW described in Section II B

A. Target design

Figure 4 shows a schematic view of the shock experiment. Targets consisted of a copper cell with a 6061-T6 aluminum buffer plate (≈250μm) and a rear Z-cut, α-quartz top-hat 1.5 mm window (single crystals, Argus International). A copper spacer ring was placed between the rear top hat and the front buffer plate. The spacer ring and top hat set the sample thickness, which was approximately 300 μm. For one experiment, the aluminum front plate was replaced with a z-cut, α-quartz buffer. The sample space was filled with high purity (>99.999%) krypton gas (Matheson Tri-Gas) to 16.8 psi and cooled to 118 K using a liquid nitrogen cryo-system[30]. Mass spectroscopy of the krypton gas verified the purity and that the krypton was of natural isotope composition. The initial liquid krypton density was calculated from a linear fit of density–temperature data[31–34] and was 2.43 g/cc with an uncertainty of 0.5%. The refractive index of liquid krypton at 118 K was (n = 1.30) determined from the experimental data of Sinnock and Smith[35]. The initial density of the aluminum drive plate at 118 K was calculated using a SESAME 3700 isobar. The flyers were aluminum 6061-T6 with initial thicknesses of 1000 μm.

B. Diagnostics and analysis

A velocity interferometer system for any reflector (VISAR)[36] was used to measure flyer (V_F) and shock (U_S) velocities with an uncertainty of 0.2% to 0.5%. Multiple VISAR signals were recorded each using different velocity per fringe settings, which eliminated 2π phase shift ambiguities upon shocks and further reduced velocity uncertainties[37]. Figure 5 shows the VISAR veloc-

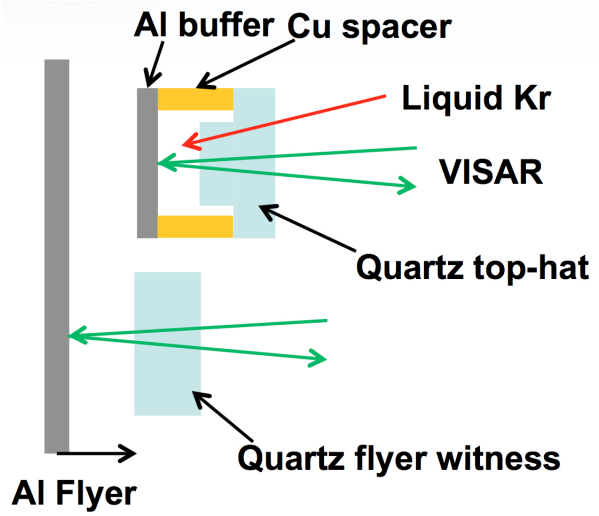

FIG. 4. Schematic of the cryogenic call used in the Z shock compression experiments; the cell allows for long (15 ns) steady shocks, see Fig. 5.

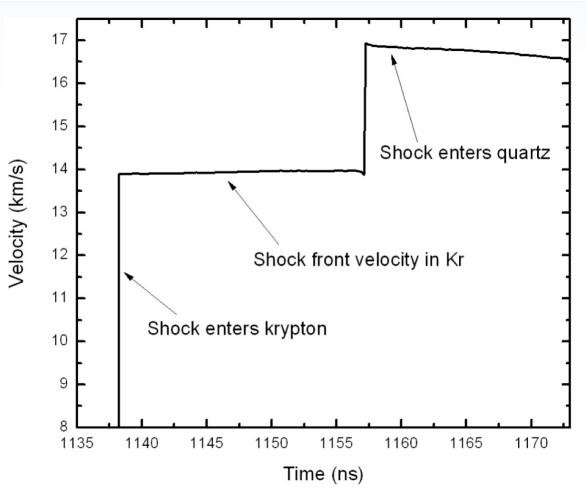

FIG. 5. Representative VISAR data. The shock transit from the aluminum drive plate into the krypton and the shock transit from the krypton to the rear quartz are indicated by sharp changes in the VISAR trace.

ity profile from one experiment. The shock front in the krypton was reflective, so as the shock transited from the aluminum buffer plate into the krypton, the shock velocity of the krypton $U_S^{\rm Kr}$ was measured directly. As an independent check on the measured shock velocity, the velocity profiles were integrated to verify that the distance travelled matched the sample thickness. Directly below the krypton target was a quartz window where the aluminum flyer velocity was measured. Some tilt can exist in the target that causes the measured flyer velocity at the quartz window and at the krypton target to differ causing scatter in the experimental data. For the experiment using the quartz buffer plate, the V_F and U_S^{Quartz} were measured directly.

The particle velocity, pressure, and density (U_P, P, and ρ) of the shock compressed krypton were calculated using a Monte Carlo impedance matching method (MCIM)[6,12] to solve the Rankine-Hugoniot equations[38]. A weighted linear fit and parameter correlation matrix for aluminum were calculated from data in Ref. 39. The aluminum Hugoniot state prior to the shock transiting into the liquid krypton was determined using the flyer velocity measured below the target on the quartz window. In each impedance match calculation, the measured shock velocities and the initial krypton density were varied about their mean using a random number with standard deviation equal to the measurement uncertainty. Uncertainty in the aluminum Hugoniot was accounted for by varying the fit parameters about their mean using correlated random numbers. The Hugoniot state was calculated using the reflected Hugoniot of aluminum and defined as the mean of the MCIM calculation with uncertainty equal to one standard deviation. The MCIM results are corrected for the aluminum release using a release isentrope calculated from SESAME 3700. The SESAME 3700 table release was shown to have good agreement with experimentally measured deep release release states for aluminum.[28] The results for the principle Hugoniot are listed in Table II. For the experiment that used α-quartz as the buffer plate, a recently developed quartz release model[40] was used in the impedance matching calculation.

The target cell geometry (Fig. 4) allowed for measurement of the reshock state in Kr. As the shock in the Kr transited into the rear quartz top-hat, the shock in the quartz becomes reflective and the quartz shock velocity was measured directly. The behavior of quartz under shock compression is well characterized,[4,40] which determined U_P and P state in the quartz and thus Kr accurately since U_P and P are equal at the boundary. The reshock state was calculated using the method described in Ref. 6 and the linear fit in Eqn. 2. Reshock results are listed in Table III.

IV. RESULTS AND DISCUSSION

Like other low impedance materials, the Kr Hugoniot data has been limited to pressures obtainable using gas guns or high-explosive drivers. In Figure 6 we show the state of knowledge before this work: experimental data was available to 90 GPa[41] and existing EOS models (SESAME 51810 and LEOS 360) exhibited markedly different behavior over this narrow range of compression. In this section, we compare the new experimental data and results from DFT/QMD simulation. The previous and newly developed tabular EOS models are compared to both sets of results over the entire pressure range along the Hugoniot.

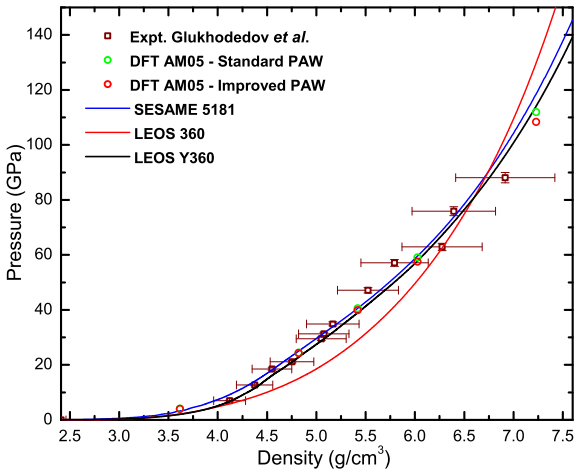

FIG. 6. Shock Hugoniot of liquid krypton below 150 GPa. Both the standard and improved PAWs show good agreement with the experimental data from Ref. 41. Th EOS tables are plotted for comparison.

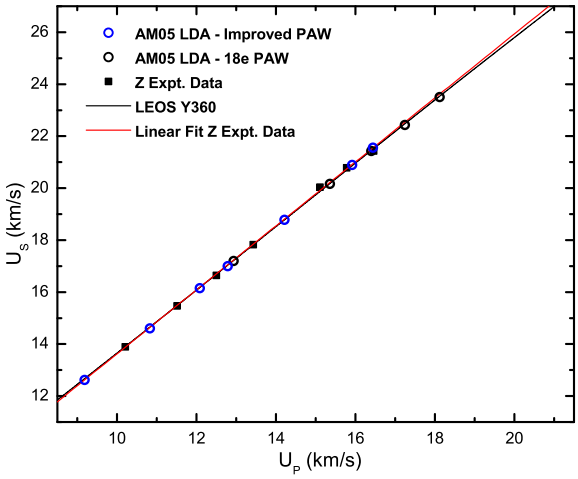

FIG. 7. Shock Hugoniot of liquid Kr in the U_S-U_P plane. The behavior is linear and the DFT calculations show good agreement with the experimental data. The Y360 EOS reproduces the data.

A. Shock Hugoniot of liquid krypton

Figs. 7 and 8 compare the Z experimental data, the tabular EOS models, and the DFT results using the improved PAW and 18-electron PAW described earlier. In the $U_S - U_P$ plane, the DFT and experimental data are in good agreement. The LEOS Y360 table reproduces both data sets up through the highest 18-electron PAW DFT data point. The weighted linear fit to the experimental data is

$$U_S = (1.313 \pm 0.225) + (1.231 \pm 0.017) U_P \qquad (2)$$

and is valid for $U_P > 9$ km/s. The off-diagonal covariance term for the fit is $\sigma_{C_0}\sigma_{S_1} = -3.834 \times 10^{-3}$.

The differences between the experimental, DFT, and tabular EOS models are more pronounced in the ρ-P plane, plotted in Fig. 8. At higher pressures, the experimental data shows scatter that is likely caused by not directly measuring the flyer plate velocity. However, the experimental and DFT results show that previous EOS models (SESAME 5181 and LEOS 360) do not describe the krypton Hugoniot at high pressures. Similarly to the liquid xenon Hugoniot[12], the previous EOS models bracket the true Hugoniot behavior likely because of their different treatments of the electronic component to the Helmholtz free energy. The LEOS Y360 table developed by Sterne[42] utilized the DFT and experimental principle Hugoniot results in its construction, thus reproducing the data.

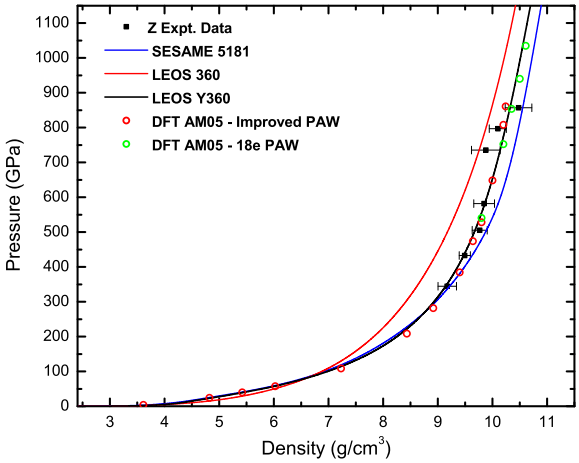

FIG. 8. Shock Hugoniot of liquid krypton in the ρ–P plane showing good agreement between the DFT calculations and experimental data while highlighting differences with existing models.

B. Reshock state in krypton

In the experiment, the Kr shock velocity (U_S) is continuously measured as the shock transits the Kr sample. At higher flyer velocities, some attenuation of the shock velocity in the Kr can occur because of release waves produced from the melted portion of the flyer. Using the linear fit to the Z experimental data (Eqn. 2) and the measured U_S, we determine the Kr pressure, density, and particle velocity prior to the shock reflecting from the Kr / quartz interface. The particle velocity and pressure in the reshock state are accurately known because they are determined from the quartz standard.[40] The Rankine-Hugoniot equations are solved to determine the Kr density in the second shock state. Table III lists the experimental observables (Kr U_S and quartz U_S) and the calculated final density and pressure state in the Kr. Figure 9 shows the Kr reshock data compared to the reshock states determined using the LEOS Y360 table.

TABLE II. Experimental data for the principal Hugoniot for shock compressed liquid krypton with an initial density of $2.43 g/cm^3$. The measured experimental quantities are the flyer velocity and the Kr shock velocity. For Z2294 the experimentally measured quantity is the shock velocity in the quartz buffer plate and Kr shock velocity.

Shot	Flyer Velocity (km/s)	U_P (km/s)	U_S (km/s)	ρ (g/cm^3)	Pressure (GPa)
Z2114	18.32 ± 0.06	10.21 ± 0.05	13.89 ± 0.05	9.172 ± 0.157	344.6 ± 2.1
Z2148	24.58 ± 0.06	13.43 ± 0.05	17.83 ± 0.07	9.847 ± 0.244	581.9 ± 3.1
Z2165	27.93 ± 0.07	15.11 ± 0.06	20.04 ± 0.04	9.878 ± 0.132	735.8 ± 3.6
Z2166	30.47 ± 0.09	16.46 ± 0.07	21.43 ± 0.09	10.478 ± 0.189	857.1 ± 5.0
Z2196	29.22 ± 0.09	15.78 ± 0.07	20.78 ± 0.04	10.099 ± 0.169	796.8 ± 4.3
Z2294-N*	21.05 ± 0.04*	11.51 ± 0.04	15.47 ± 0.03	9.494 ± 0.103	432.7 ± 2.0
Z2294-S*	22.96 ± 0.04*	12.50 ± 0.04	16.64 ± 0.05	9.770 ± 0.138	505.5 ± 2.4

* Indicates experiments that used a quartz drive plate. The listed velocity is the shock velocity in the quartz.

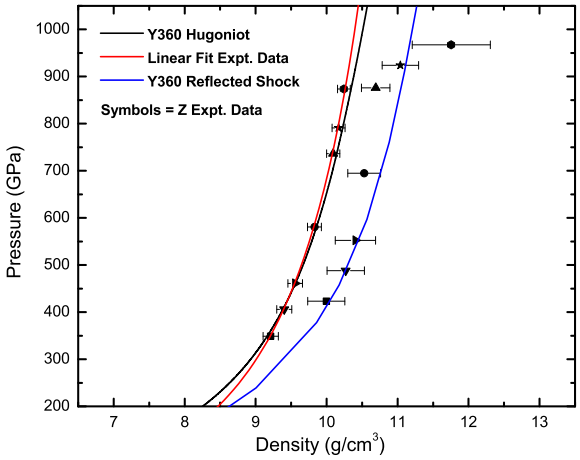

FIG. 9. The experimental reshock data and calculated reshock envelope using the LEOS Y360 EOS table and quartz hugoniot[40]. The different symbols connect measurements from the same experiment, for instance the shock state marked by the square at ≈ 345 GPa and 9.2 g/cc was the intial state for the reshock measurement also marked by a square at ≈ 423 GPa and 10.0 g/cc. The re-shock state probes compression at higher density (lower temperature) than the corresponding first shock state. Again, the LEOS Y360 t¡able performs well, capturing the re-shock states.

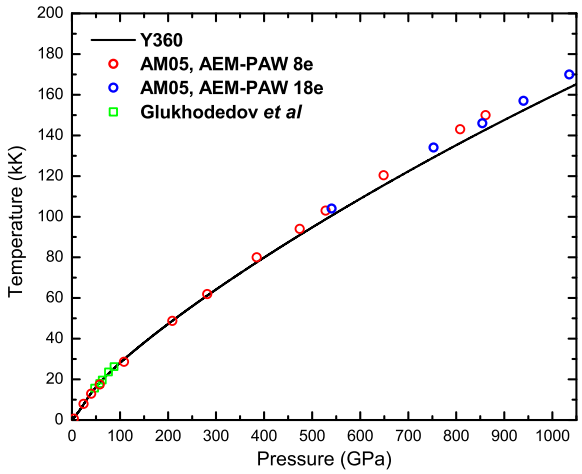

FIG. 10. Temperature along the Hugoniot for liquid krypton: experimental data[41], DFT/QMD results, and calculated from the Y360 tabular EOS. The difference between DFT/QMD and Y360 increases with pressure although it remains smaller than 5% also at 1000 GPa/ 160 kK.

Reshock paths are calculated using the Y360 table and impedance matching to the quartz Hugoniot to determine the reshock envelope of states. The Y360 EOS shows good agreement over the examined pressure range, a sign that the EOS table is valid along the principal Hugoniot and also for off Hugoniot states reached via repeated shocks.

C. Shock temperature of liquid krypton

The temperature of shocked material is of great importance, but subject to significant uncertainties due to lack of experimental data. Results from QMD simulations are often the only temperature information available. It is therefore of importance to compare QMD based estimations of temperature of shock states with EOS tables/models. Figure 10 plots the Hugoniot temperature calculated using the Y360 EOS table and the DFT temperatures. The EOS model and DFT temperatures show good agreement over the examined pressure range-better than 5% for pressures below 1000 GPa. The agreement suggests that the thermal models used in design of Y360 are appropriate for this pressure range.

D. Equation of State Models

The difficulty in describing high energy density materials at several Mbar without the use of first-principles simulations like QMD is evident from the behavior of the different models shown in Figs 6 and 8. Traditionally, EOS models are calibrated Hugoniot data from plate impact experiments and isothermal data from diamond anvil cells (DAC). Extrapolation beyond the range of experiments is challenging. Most expressions for the free energy of a material utilize a separation between contributions from cold compression (the cold curve), thermal excitations of ions (ionic thermal model), and finally the contribution of thermal excitations of electrons (elec-

TABLE III. Experimental data for the reshock state in liquid krypton with an initial density of $2.43 g/cm^3$.

Shot	Kr U_S (km/s)	Quartz U_S (km/s)	Kr ρ (g/cm^3)	Kr Pressure (GPa)
Z2114	13.96 ± 0.04	16.86 ± 0.03	9.996 ± 0.261	423.4 ± 1.8
Z2148	17.82 ± 0.05	20.92 ± 0.04	10.530 ± 0.231	694.7 ± 3.1
Z2165	19.98 ± 0.04	23.14 ± 0.05	10.692 ± 0.201	876.0 ± 4.4
Z2166	21.41 ± 0.09	24.16 ± 0.07	11.756 ± 0.549	967.2 ± 6.5
Z2196	20.68 ± 0.05	23.68 ± 0.05	11.039 ± 0.256	923.7 ± 4.5
Z2294-N	15.01 ± 0.03	17.94 ± 0.04	10.270 ± 0.264	488.2 ± 2.5
Z2294-S	15.95 ± 0.05	18.93 ± 0.05	10.406 ± 0.284	552.2 ± 3.4

tronic thermal model). The problem is under-constrained in terms of experimental data, especially the thermal terms due to the lack of high-precision temperature measurements at high pressure conditions. The resulting EOS is based on a separation of terms in the free energy that is not unique. While the combined behavior in pressure and energy leading to the Hugoniot condition is constrained by experiments, the behavior of different terms with pressure and temperature is not, often resulting in strong deviations between different EOS models as they are extrapolated to pressures of hundreds of GPa.

In the case of Kr, we find that the Y360 table reproduces the principal Hugoniot data over a wide range and also captures off-Hugoniot data as shown in Fig. 9. The Y360 table temperatures are also consistent with the QMD results over a wide range and thus we find that Y360 should be the preferred equation of state for Kr under high energy density conditions.

V. SUMMARY

We have performed an extensive study of shock compressed liquid krypton up to 850 GPa on first shock and 950 GPa on re-shock. Integration of DFT calculations and shock experiments provides a solid basis for understanding the behavior of krypton at extreme conditions. We demonstrate that QMD simulations can be performed with high precision also at temperatures above 10 eV (110 kK) provided that the high-energy scattering properties of the pseudopotentials/core potentials are verified. Furthermore, we find that the exchange-correlation functional AM05 captures the energetic variations in a cryogenic krypton liquid as calculated with quantum Monte Carlo, making it a good choice for krypton. The use of high-fidelity first-principles simulations allows for a significantly more detailed understanding of the different components of the free energy. QMD straightforwardly yields internal energy, pressure, structure, diffusion, and the entropy for solids. Recently, a method was developed that yields entropy[43] with very high precision, making QMD a complete method for first-principles thermodynamics. Successful application of QMD to thermodynamics, however, relies on performing converged simulations, using core-potentials of high fidelity for high temperature applications, and informed choices of exchange-correlation functionals.

VI. ACKNOWLEDGEMENTS

The authors thank all members of the Sandia Z-facility that contributed to the design, fabrication, and fielding of the Z experiments. The authors especially appreciate the dedicated efforts of the cryo-team: Andrew Lopez, Jesse Lynch, Jose Villalva, and Keegan Shelton as well as the engineering designs by Devon Dalton and the diagnostics by Charlie Meyer. The work was supported by the NNSA Science Campaigns. LS was also supported through the Predictive Theory and Modeling for Materials and Chemical Science program by the Office of Basic Energy Science (BES), Department of Energy (DOE).

Sandia National Laboratories is a multi-program laboratory operated by Sandia Corporation, a wholly owned subsidiary of Lockheed Martin Company, for the U.S. Department of Energy's National Nuclear Security Administration under Contract No. DE-AC04-94AL85000.

* trmatts@sandia.gov
† sroot@sandia.gov
‡ aematts@sandia.gov
§ lshulen@sandia.gov
¶ rjmagya@sandia.gov
** dgflick@sandia.gov

[1] P. Hohenberg and W. Kohn, Phys. Rev. **136**, B864 (1964); W. Kohn and L. J. Sham, Phys. Rev. **140**, A1133 (1965).
[2] M. Desjarlais, Phys. Rev. B **68**, 064204 (2003).
[3] M. D. Knudson, M. P. Desjarlais, and D. H. Dolan, Science **322**, 1822 (2008).
[4] M. D. Knudson and M. P. Desjarlais, Phy. Rev. Lett. **103**, 225501 (2009).
[5] M. D. Knudson, M. P. Desjarlais, R. W. Lemke, T. R. Mattsson, M. French, N. Nettelmann, and R. Redmer, Phys. Rev. Lett. **108**, 091102 (2012).
[6] S. Root, K. R. Cochrane, J. H. Carpenter, and T. R. Mattsson, Phys. Rev. B **87**, 224102 (2013).
[7] A. E. Mattsson, P. A. Schultz, M. P. Desjarlais, T. R. Mattsson, and K. Leung, Modelling Simul. Mater. Sci. Eng. **13**, R1 (2005).
[8] R. Armiento and A. E. Mattsson, Phys. Rev. B **72**, 085108

(2005).
[9] W. Kohn and A. E. Mattsson, Phys. Rev. Lett. **81**, 3487 (1998).
[10] A. E. Mattsson, R. Armiento, J. Paier, G. Kresse, J. M. Wills, and T. R. Mattsson, J. Chem. Phys. **128**, 084714 (2008).
[11] P. Haas, F. Tran, and P. Blaha, Phys. Rev. B **79**, 085104 (2009).
[12] S. Root, R. J. Magyar, J. H. Carpenter, D. L. Hanson, and T. R. Mattsson, Phys. Rev. Lett. **105**, 085501 (2010).
[13] L. Shulenburger and T. R. Mattsson, Phys. Rev. B **88**, 245117 (2013).
[14] A. Benali, L. Shulenburger, N. A. Romero, J. Kim, and O. A. von Lilienfeld, Journal of Chemical Theory and Computation **0**, 0 (2014).
[15] G. L. Pollack, Rev. Mod. Phys. **36**, 748 (1964).
[16] D. L. Losee and R. O. Simmons, Phys. Rev. **172**, 944 (1968).
[17] J. P. Perdew and A. Zunger, Phys. Rev. B **23**, 5048 (1981).
[18] J. Kim, K. P. Esler, J. McMinis, M. A. Morales, B. K. Clark, L. Shulenburger, and D. M. Ceperley, Journal of Physics: Conference Series **402**, 012008 (2012).
[19] M. A. Morales, J. R. Gergely, J. McMinis, J. M. McMahon, J. Kim, and D. M. Ceperley, Journal of Chemical Theory and Computation **0**, 0 (2014), http://pubs.acs.org/doi/pdf/10.1021/ct500129p.
[20] R. C. C. III, J. B. McMinis, J. M. McMahon, C. Pierleoni, D. M. Ceperley, and M. A. Morales, Phys. Rev. B **89**, 184106 (2014).
[21] P. E. Blöchl, Phys. Rev. B **50**, 17953 (1994); G. Kresse and D. Joubert, Phys. Rev. B **59**, 1758 (1999).
[22] T. R. Mattsson and R. J. Magyar, in *Shock Compression of Condensed Matter – 2009*, AIP Conf. Proc., Vol. 1195, edited by M. L. Elert *et al.* (AIP, Melville, New York, 2009) pp. 797–800.
[23] A. E. Mattsson, *A lithium projector augmented wave potential suitable for use in VASP at high compression and temperature*, Technical report SAND2012-7389 (Sandia National Laboratories, Albuquerque, New Mexico 87185 and Livermore, California 94550, 2012).
[24] G. Kresse and J. Hafner, Phys. Rev. B **47**, R558 (1993), Phys. Rev. B **49**, 14251 (1994); G. Kresse and J. Furthmüller, Phys. Rev. B **54**, 11169 (1996).
[25] N. Mermin, Phys. Rev. **137**, A1441 (1965).
[26] M. E. Savage, L. Bennett, D. Bliss, W. Clark, R. Coats, J. Elizondo, K. LeChien, H. Harjes, J. Lehr, J. Maenchen, D. McDaniel, M. Pasik, T. Pointon, A. Owen, D. Seidel, D. Smith, B. Stoltzfus, K. Struve, L. Warne, J. Woodworth, C. Mendel, K. Prestwich, R. Shoup, and D. Johnson, in *2007 IEEE Pulsed Power Conference*, Vol. 1-4 (2007) p. 979.
[27] R. Lemke, M. Knudson, D. Bliss, K. Cochrane, J.-P. Davis, A. Giunta, H. Harjes, and S. Slutz, J. Appl. Phys. **98**, 073530 (2005).
[28] M. D. Knudson, J. R. Asay, and C. Deeney, J. Appl. Phys. **97**, 073514 (2005).
[29] S. Root, T. A. Haill, J. M. D. Lane, A. P. Thompson, G. S. Grest, D. G. Schroen, and T. R. Mattsson, Journal of Applied Physics **114**, 103502 (2013).
[30] D. Hanson, R. Johnson, M. Knudson, J. Asay, C. Hall, J. Bailey, and R. Hickman, in *Shock Compression of Condensed Matter – 2001*, AIP Conf. Proc., Vol. 620, edited by M. D. Furnish, N. N. Thadhani, and Y. Horie (AIP, Melville, New York, 2001) p. 1141.
[31] A. C. Hollis-Hallet, in *Argon, Helium, and the Rare Gases*, Vol. 1, edited by G. A. Cook (Interscience Publishers, Inc., New York, 1961) Chap. 9, p. 359.
[32] G. T. Clayton and L. Heaton, Phys. Rev. **121**, 649 (1961).
[33] M. J. Terry, J. T. Lynch, M. Bunclark, K. R. Mansell, and L. A. K. Staveley, J. Chem. Thermodynamics **1**, 413 (1969).
[34] C. Gladun and F. Menzel, Cryogenics **10**, 210 (1970).
[35] A. C. Sinnock and B. L. Smith, Phys. Rev. **181**, 1297 (1969).
[36] L. M. Barker and R. E. Hollenbach, J. Appl. Phys. **43**, 4669 (1972).
[37] D. H. Dolan, *Foundations of VISAR analysis*, Technical report SAND2006-1950 (Sandia National Laboratories, Albuquerque, New Mexico 87185 and Livermore, California 94550, 2006).
[38] G. E. Duvall and R. A. Graham, Rev. Mod. Phys. **49**, 523 (1977).
[39] M. D. Knudson, R. Lemke, D. Hayes, C. A. Hall, C. Deeney, and J. Asay, J. Appl. Phys. **94**, 4420 (2003).
[40] M. D. Knudson and M. P. Desjarlais, Phys. Rev. B **88**, 184107 (2013).
[41] V. D. Glukhodedov, S. I. Kirshanov, T. S. Lebedeva, and M. A. Mochalov, J. Expt. Theoretical Phys. **89**, 292 (1999).
[42] P. A. Sterne, (2013), *Private Communication*.
[43] M. P. Desjarlais, Phys. Rev .B **88**, 062145 (2013).